aerospace

MDPI

Article

KISP Hand: Space Gripper for On-Orbit Servicing Missions

Taewon Choi [1,2], Daehee Won [1,2], Byung-Rok So [1,2] and Dong-Hyuk Lee [1,2,*]

[1] Human-Centric Robotics R&D Department, Korea Institute of Industrial Technology (KITECH), Ansan 15588, Republic of Korea; macintosh9201@kitech.re.kr (T.C.); daehee@kitech.re.kr (D.W.); newmal@kitech.re.kr (B.-R.S.)

[2] Robotics Engineering Department, University of Science and Technology (UST), Daejeon 34113, Republic of Korea

* Correspondence: donghyuk@kitech.re.kr

Abstract

In this paper, an engineering model (EM) of a multi-joint space gripper for on-orbit servicing (OOS) is proposed. OOS missions demand robotic systems capable of reliable physical interactions under dynamic uncertainties and harsh space environments. While prior space-qualified grippers have demonstrated dexterous manipulation through anthropomorphic, high-DoF configurations, this work adopts a design direction widely established in industrial applications: a three-finger, lower-DoF configuration that balances grasp versatility, structural simplicity, and system integration for OOS missions. The developed gripper features a tendon-driven mechanism with a structural design optimized for space-environment compatibility and mechanical compliance. The kinematic characteristics of the mechanism are analyzed, while workspace and manipulability analyses are conducted to evaluate its operational limits. To verify the functional feasibility of the proposed design, representative grasping experiments were performed using a fabricated EM. The mechanical reliability and grasping performance were evaluated through a series of empirical experiments. The results indicate that the proposed design achieves a practical balance among grasp versatility, structural simplicity, and system integration for OOS missions, with a shielding-oriented structural configuration adopted as a design baseline. Its functional feasibility is supported by kinematic analysis, repeatability verification, and grasping experiments. This study provides a basis for the design and evaluation of three-finger robotic grippers in future OOS missions.

Keywords: space robotics; on-orbit servicing; robot gripper; space applications

Check for updates

Academic Editor: Jun He

Received: 23 April 2026
Revised: 20 May 2026
Accepted: 29 May 2026
Published: 31 May 2026

Copyright: © 2026 by the authors. Licensee MDPI, Basel, Switzerland. This article is an open access article distributed under the terms and conditions of the Creative Commons Attribution (CC BY) license.

1. Introduction

On-orbit servicing (OOS) refers to a set of technologies that provide inspection, maintenance, refueling, relocation, and removal services for uncrewed space objects—such as artificial satellites, space structures, and orbital debris—directly in outer space [1]. As humanity increasingly utilizes low Earth orbit (LEO) and geostationary orbit (GEO), extending the operational lifespan of satellites and ensuring the long-term sustainability of the space environment have emerged as critical challenges. In particular, the growing number of aging satellites and the rapid increase in space debris—both of which elevate the risk of on-orbit collisions—are now recognized as serious issues in the context of space traffic management and sustainable space utilization [2].

Conventional approaches have considered crewed missions involving astronauts to address these challenges [3]. However, crewed servicing is inherently constrained by the

substantial cost and operational complexity associated with life-support infrastructure, as well as the biological vulnerabilities of astronauts to space radiation and microgravity-induced physiological degradation [4,5].

Consequently, space agencies and private enterprises worldwide have increasingly recognized robotics-based OOS technologies as a viable alternative and are actively advancing missions based on autonomous and remotely operated systems [4]. In this context, space robotics research has primarily focused on the kinematic and dynamic design of manipulators, control stability in zero-gravity environments, and strategies for approaching and capturing non-cooperative targets [6–8]. However, comparatively less emphasis has been placed on the physical design and experimental validation of the gripper (end-effector) mounted at the distal end of the manipulator. The gripper constitutes a critical component in OOS missions, as it directly interacts with target objects and significantly influences capture stability, operational precision, and overall mission success [9,10]. The space environment imposes fundamentally different requirements from terrestrial conditions, including vacuum, extreme temperature variations, radiation exposure, and constrained power and communication resources [11].

These constraints necessitate careful consideration of structural reliability, actuation mechanisms, and electronic system architecture to ensure compatibility with space conditions [12]. Many prior space robotic grippers have been designed with anthropomorphic characteristics, often employing high degrees of freedom (DoF) to achieve human-like dexterity [9,10]. However, such high-DoF systems inherently introduce increased complexity in actuation and control [13,14]. Meanwhile, previous studies have demonstrated that a wide range of manipulation tasks can be effectively performed using lower-DoF configurations [15–17]. From this perspective, the KISP Hand is designed to achieve a controlled trade-off between grasp versatility, structural simplicity, and system integration. These characteristics are particularly advantageous in space environments, where reliability is critical because of limited resources and harsh conditions. Furthermore, three-finger grippers can provide multiple grasping modes while maintaining mechanical efficiency and adaptability, supporting their applicability to both industrial and space robotic systems.

Accordingly, this study presents the KISP Hand (KItech SPace Hand), a three-finger multi-joint gripper intended for OOS missions. The proposed gripper is developed based on a mechanical structure and electronic system architecture tailored for space environments. In particular, it integrates a customized actuation mechanism and a 4 mm aluminum shielding strategy to protect radiation-sensitive electronic components while maintaining sufficient dexterity to achieve stable grasping of irregular and non-cooperative targets. A conceptual illustration of the proposed KISP Hand operating in an on-orbit servicing environment is presented in Figure 1.

To position the proposed design relative to existing space-qualified grippers, Table 1 compares representative prior systems with the KISP Hand in terms of finger number, DoF, mass, workspace volume, radiation-related design strategy, and reference information.

As shown in Table 1, several key performance indices (e.g., workspace volume, manipulability) are not consistently reported across prior space-qualified grippers, which precludes a fully aligned quantitative comparison. This reporting gap itself motivates the present work to provide a self-contained kinematic and experimental characterization of the KISP Hand—including workspace volume, manipulability distribution, repeatability, and grasping success rate—as documented in Sections 3 and 4. The intent of Table 1 is therefore to position the KISP Hand within the design-space spanned by prior space-qualified grippers along commonly reported axes (finger count, DoF, mass, and shielding strategy), rather than to claim quantitative superiority along any single axis.



Figure 1. Conceptual illustration of the proposed KISP Hand operating in orbit. This figure is a conceptual representation and does not constitute a technical drawing of the proposed system. The image was composed by the authors and refined using Gemini (Background image source: NASA/GSFC, Image No. WEB14529-2014).

Table 1. Comparison of representative space-oriented multi-fingered grippers and the proposed KISP Hand (N/R: Not Reported in the original publication).

Gripper	Fingers	DoF	Mass	Workspace Vol.	Radiation Strategy	Ref.
DexHand	4	12	4.00 kg	N/R	2 mm Al shell; 120 Gy tested	[9,18]
SpaceHand	4	12	5.00 kg	N/R	Al shell; 50 kRad /5-yr GEO	[10,19]
Cosmic Gripper-1	3	12	3.24 kg	1.08×10^{-2} m^3	4 mm Al shell	[12]
KISP Hand	3	9	5.80 kg	1.31×10^{-2} m^3	4 mm Al shell	This work

As summarized in Table 1, prior space-oriented multi-fingered grippers have generally employed relatively high-DoF configurations to achieve dexterous manipulation. In contrast, the KISP Hand adopts a 3-finger, 9-DoF configuration that does not simply increase the number of DoF, but instead aims to balance grasp versatility, structural simplicity, system integration efficiency, and radiation-shielding feasibility. Despite its lower DoF count relative to the representative prior systems, the KISP Hand provides a workspace volume on the same order as the only previously reported prior system for which this metric is reported (Cosmic Gripper-1, Table 1), while incorporating a 4 mm aluminum shielding structure for electronic protection.

Based on the above positioning, the principal contributions of this work are summarized as follows:

- Design Concept and Direction: Proposal of the design concept and direction for the KISP Hand, a multi-joint gripper intended for OOS missions.
- Radiation Shielding and Hardware Design: Development of a shielding-oriented structural baseline for reducing radiation exposure to internal electronic components, with quantitative limitations identified for EQM-level reinforcement.
- Kinematic Performance Characterization: Numerical verification of the gripper's kinematic performance, including its workspace and manipulability.

- Functional Performance Validation: Presentation of experimental results demonstrating the practical grasping capabilities of the fabricated engineering model (EM) on unstructured objects.

By focusing on the physical design and experimental validation of an OOS gripper, this study provides a design and evaluation basis for future space-oriented robotic end-effectors operating in constrained and harsh space environments.

2. System Details

This section provides a detailed description of the EM of the KISP Hand, a multi-joint robotic hand designed for OOS missions. In space environments, the stable operation of mechanical and electronic components requires careful consideration of both radiation shielding and resistance to extreme temperature variations. The present study places particular emphasis on radiation-shielding feasibility at the structural-design level, proposing a design strategy intended to provide a shielding-ready baseline while suppressing the payload mass increase caused by the use of heavy shielding materials. Quantitative validation of the resulting shielding performance is positioned as part of the subsequent EQM verification campaign (Section 5.3).

The proposed gripper incorporates the following structural features to minimize radiation exposure and maximize actuation reliability. First, a tendon-driven actuation method—in which the term tendon refers to a flexible cable transmitting force between a remote actuator and the driven joint—was adopted, allowing critical electrical components, such as actuators and the main control board, to be centralized within a secure internal compartment of the spacecraft. Robotic joint actuation can be broadly classified into direct-drive and indirect-drive methods; the tendon-driven mechanism is a representative indirect method in which the joints and actuators are physically separated, offering the advantage of high design flexibility [20–22]. Through this approach, only purely mechanical elements—namely, the links and tendons—are exposed to the external space environment. Second, to minimize the number of electrical components exposed to space, additional sensors were excluded, relying solely on motor encoders. Third, the material and thickness of the gripper base structure were optimized based on prior research analyzing radiation attenuation models in LEO environments [23–27], thereby minimizing the overall mass increase of the system while providing a shielding-oriented structural baseline for subsequent EQM-level radiation reinforcement.

2.1. Design

The design of the KISP Hand prioritizes the realization of optimal grasping performance for OOS missions while simultaneously ensuring adequate space radiation shielding capability. Conventional grippers typically employ either a direct-drive configuration, where motors are mounted directly at the joints [28], or a linkage-based mechanism for power transmission [29]. However, direct-drive systems tend to increase the size and mass of finger joints, thereby limiting precision in fine manipulation tasks. Meanwhile, linkage-based systems—while mechanically robust—suffer from a rapid increase in structural complexity when implementing multiple DoF [29]. In particular, the scarcity of space-qualified ball screw components, which are essential for linkage-based actuation, poses a significant hurdle for space applications.

To address these challenges, a tendon-driven actuation approach was adopted for this design. This method offers several distinct advantages:

- Spatial Separation: It enables the physical separation of actuators and joints, facilitating the optimization of finger size and mass.

- System Reliability: The relatively simple mechanical structure allows for the integration of existing space-qualified motors while maintaining high system reliability.
- Design Flexibility: With the incorporation of appropriate control compensation algorithms, the tendon-driven approach provides enhanced flexibility in achieving multiple DoF compared to conventional linkage mechanisms.
- Shielding Optimization: By centralizing the heavy drive components, this architecture makes it significantly easier to implement spot shielding—using materials like CFRP/W/CFRP or polyethylene—to protect sensitive electronics from proton radiation in future engineering qualification model (EQM) developments.

The overall configuration of the KISP Hand is illustrated in Figure 2A, and its key specifications are summarized in Table 2. The detailed structure of the aforementioned radiation shielding design is shown in Figure 2B. Previous studies on space radiation shielding suggest that a 4 mm thick aluminum layer can provide a practical shielding baseline under representative orbital radiation conditions [23]. Based on these findings, the proposed gripper is designed such that radiation-sensitive electronic components are internally concentrated and enclosed by a 4 mm thick aluminum housing.

Table 2. Specifications of the engineering model.

Component	Specification
Palm Housing Material	Aluminum
Finger Housing Material	PA12
Motor	Maxon DCX 22S
Tendon Cable	0.89 mm UHMWPE fiber (Spectra®, Honeywell International Inc., Morristown, NJ, USA)
Torsion Spring (Intermediate Joints)	3.81 N·mm/deg
Torsion Spring (Distal Joints)	1.88 N·mm/deg
Total System Weight	5.8 kg (Without tool changer)

This thickness was selected with an additional margin relative to comparable space-qualified grippers (e.g., DexHand: 2 mm Al [9,18]; see Table 1), in anticipation of localized shielding non-uniformity that may arise from cable interfaces, cover-plate gaps, connectors, and structural openings inherent to the as-built cavity geometry.

At the connector-interface level, this concern is partially mitigated through the selection of high-reliability connectors with documented space-application properties (see Section 2.4).

The 4 mm aluminum specification adopted in this work is positioned as a literature-grounded shielding baseline, drawing on prior analytical studies of aluminum attenuation in LEO/GEO environments [23–27] that provide first-order justification for the selected thickness under representative mission profiles. This literature-grounded approach is consistent with the design practice reported for comparable space-qualified multi-fingered grippers such as DexHand [9,18] and SpaceHand [10,19], in which the aluminum shell thickness is similarly specified on the basis of mission-level dose estimates and component-level radiation testing. A detailed characterization of the as-built cavity geometry—including the localized shielding non-uniformity at cable interfaces, cover-plate gaps, connectors, and structural openings—is positioned as part of the subsequent EQM verification campaign described in Section 5.3.

Additionally, in our previous work developing a space gripper with a tendon-driven mechanism [12], frequent disconnections of motor and encoder cables were observed due to friction within the confined internal space. To resolve this issue, the proposed

design incorporates a structured routing system that bundles the motor and encoder cables together before safely directing them to the control board.

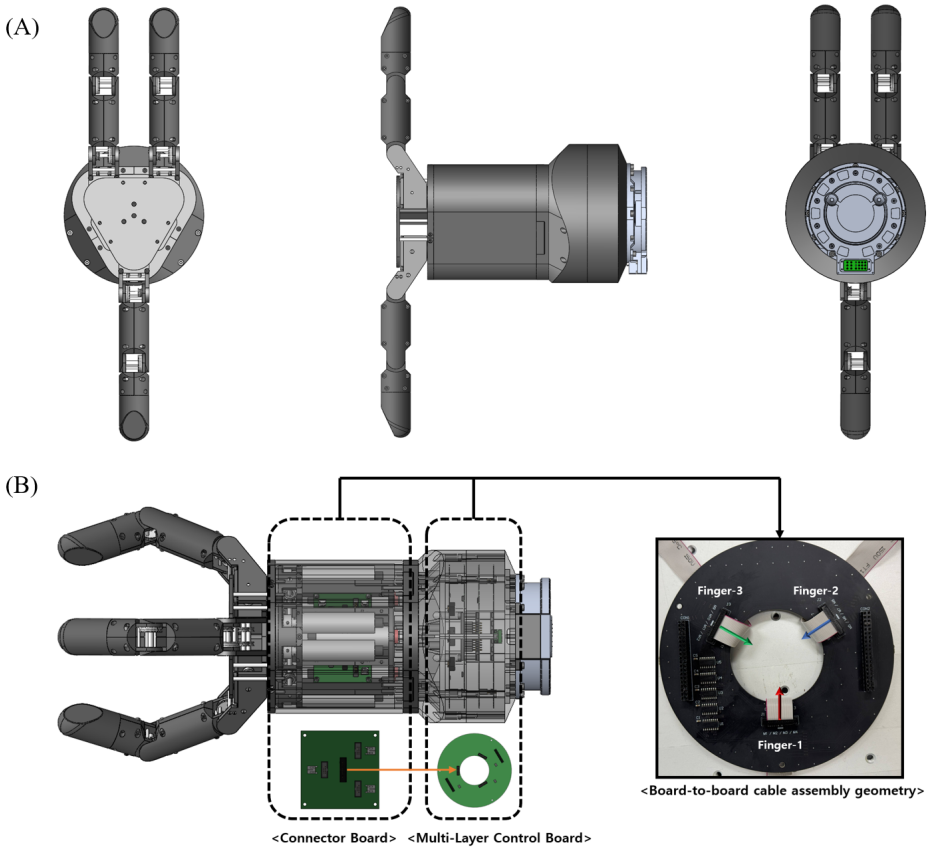


Figure 2. 3D CAD graphic images of the KISP Hand, showing the symmetric 120° inter-finger spacing around the palm center (**A**). Radiation shielding design and inter-board connection structure (**B**).

Through this structural modification, the durability issues inherent in conventional tendon-driven grippers have been mitigated, and this improved cable routing configuration is also depicted in Figure 2B.

2.2. Details of Tendon-Driven System

The proposed gripper adopts an open-chain, tendon-driven actuation system [12,30], which is inherently advantageous for radiation shielding by allowing the actuators to be positioned within the protected base.

The kinematic relationships are derived for a single finger, since all three fingers share an identical mechanical structure. The symbols and parameters used for the tendon-driven system are defined in Table 3. Let q_1, q_2, and q_3 denote the angular positions of the metacarpophalangeal (MCP), proximal interphalangeal (PIP), and distal interphalangeal (DIP) joints of a single finger, respectively. The corresponding motor positions driving these joints are defined as m_1, m_2, and m_3 (see Figure 3).

Table 3. Definitions of symbols used in the tendon-driven system.

Symbol	Unit	Description
$m_{1,2,3}$	rad	Motor angle position for a single finger
$q_{1,2,3}$	rad	Joint angle positions corresponding to MCP (metacarpophalangeal), PIP (proximal interphalangeal), and DIP (distal interphalangeal) joints
$l_{1,2}$	mm	Length of each tendon cable
$r_{m,b,j}$	mm	Radius of the motor pulley, grooved bearing, and joint pulley

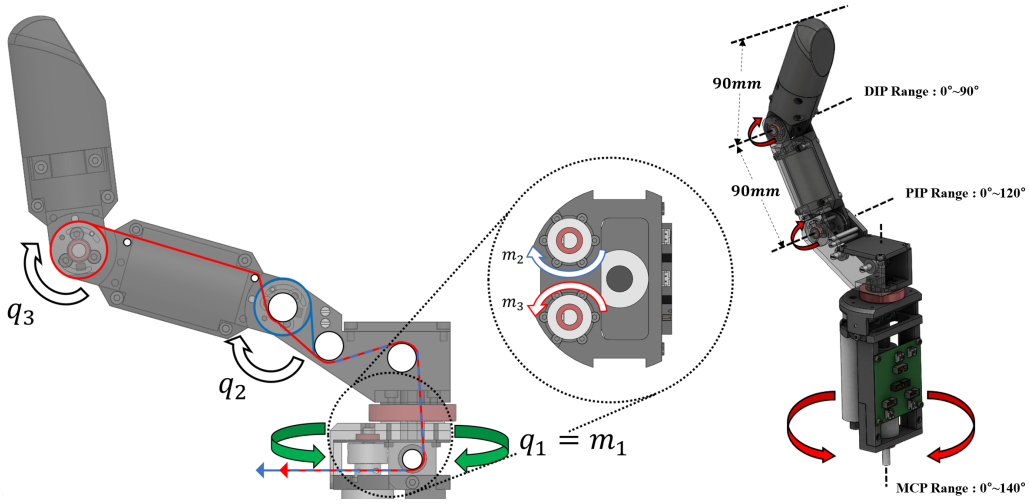


Figure 3. Details of the tendon-driven system in KISP Hand's finger module.

First, the MCP joint (q_1) is directly actuated by its dedicated motor, resulting in a linear displacement relationship:

$$\Delta q_1 = \Delta m_1 \tag{1}$$

In contrast, the PIP and DIP joints are driven via tendon-pulley mechanisms. The transmission ratio is determined by the radii of the motor pulley (r_m) and the joint pulley (r_j). For the PIP joint (q_2), the relationship is purely dependent on this ratio:

$$\Delta q_2 = \frac{r_m}{r_j} \Delta m_2 \tag{2}$$

Given the design parameters $r_m = 5.5\,\text{mm}$ and $r_j = 11\,\text{mm}$, the reduction ratio is 0.5, yielding $\Delta q_2 = 0.5\Delta m_2$. For the DIP joint ($q_3$), a kinematic coupling effect occurs because its tendon is routed over the grooved bearing (r_b) of the PIP joint. Therefore, the total angular displacement of the DIP joint (Δq_3) is the superposition of the coupled displacement induced by the PIP joint's motion ($\Delta q_{3,c}$) and the independent displacement driven by its own motor ($\Delta q_{3,i}$):

$$\Delta q_3 = \Delta q_{3,c} + \Delta q_{3,i} \tag{3}$$

The coupled displacement $\Delta q_{3,c}$ is caused by the change in tendon length as it wraps around the grooved bearing of the PIP joint. A CAD-based geometric analysis (detailed in Appendix A) showed that a maximum PIP joint rotation of 120° produces a 123.62° change in the tendon wrap angle around the grooved bearing, arising from the non-coincident placement of the PIP rotation axis and the bearing center. Applying this geometric coupling factor ($k = 123.62/120 \approx 1.03$), the coupled term is defined as:

$$\Delta q_{3,c} = k\left(\frac{r_b}{r_j}\right)\Delta q_2 \approx 1.03\left(\frac{r_b}{r_j}\right)\Delta q_2 \tag{4}$$

By substituting the specified design values ($r_b = 4.5\,\text{mm}$, $r_j = 11\,\text{mm}$) and combining them with the independent actuation term ($\Delta q_{3,i} = \frac{r_m}{r_j}\Delta m_3$), the final displacement equation for the DIP joint is derived as follows:

$$\Delta q_3 = 0.211\Delta m_2 + 0.5\Delta m_3 \tag{5}$$

Finally, the overall kinematic relationship between the joint displacements and the motor actuations for a single finger module can be summarized in matrix form:

$$\begin{bmatrix} \Delta q_1 \\ \Delta q_2 \\ \Delta q_3 \end{bmatrix} = \begin{bmatrix} 1 & 0 & 0 \\ 0 & 0.5 & 0 \\ 0 & 0.211 & 0.5 \end{bmatrix} \begin{bmatrix} \Delta m_1 \\ \Delta m_2 \\ \Delta m_3 \end{bmatrix} \tag{6}$$

The experimental validation of the finger actuation, based on the kinematic relationship derived in Equation (6), is detailed in Section 4.

2.3. Kinematic Modeling of a Single Finger

2.3.1. Forward Kinematics

Since the three fingers of the KISP Hand share an identical mechanical structure and are symmetrically arranged at 120° intervals around the palm center, the kinematic behavior of the entire hand can be characterized by analyzing a single finger and replicating the result through a base-frame rotation. Each finger consists of three serially connected revolute joints, namely the MCP, PIP, and DIP joints, whose angles are denoted by q_1, q_2, and q_3, respectively.

Let L_1 denote the offset from the palm-base frame $\{O\}$ to the MCP joint along the x-axis, and L_2 denote the rigid offset from the MCP joint to the PIP joint. Let L_3 and L_4 denote the lengths of the proximal and distal phalanges, respectively. The fingertip position $\mathbf{p}_{Tip} = [x_{Tip}, y_{Tip}, z_{Tip}]^T$, expressed in the palm-base frame $\{O\}$, is then given by Equation (7),

$$\begin{aligned} x_{tip} &= L_1 + \left[L_2 + L_3 \cos q_2 + L_4 \cos(q_2 + q_3)\right] \cos q_1, \\ y_{tip} &= \quad\; \left[L_2 + L_3 \cos q_2 + L_4 \cos(q_2 + q_3)\right] \sin q_1, \\ z_{tip} &= L_3 \sin q_2 + L_4 \sin(q_2 + q_3) \end{aligned} \tag{7}$$

Here, $L_1 = 45\,\text{mm}$, $L_2 = 55\,\text{mm}$, $L_3 = 90\,\text{mm}$, and $L_4 = 81\,\text{mm}$ (see Figure 4). The same expression applies to all three fingers up to a rotation about the palm normal corresponding to the symmetric 120° arrangement. The subsequent derivations are presented for a single representative finger.

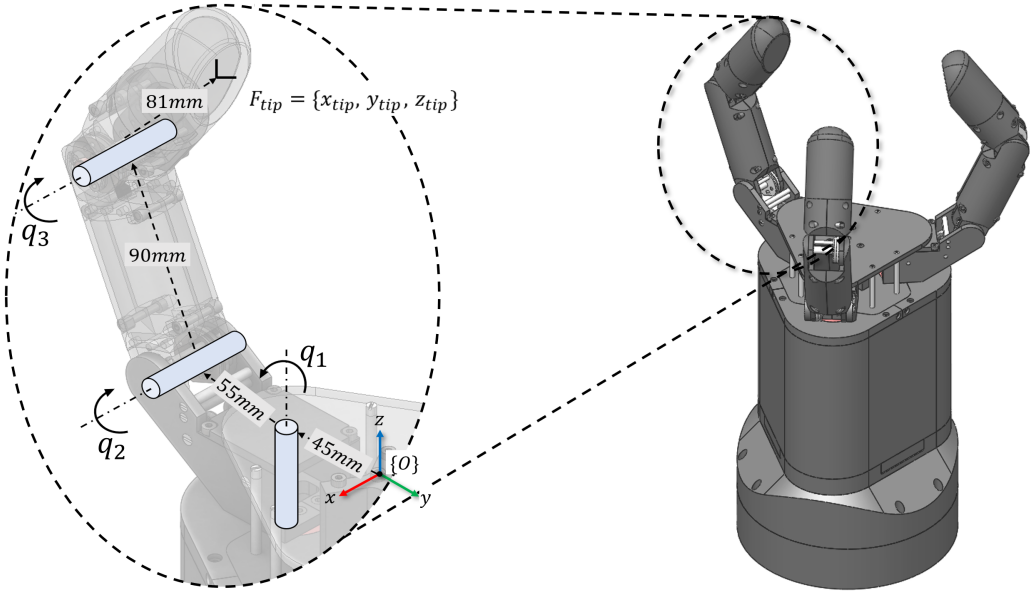


Figure 4. Kinematic parameters and reference frames of a single finger module, with the symmetric three-finger arrangement of the KISP Hand shown on the right.

2.3.2. Jacobian Matrix

The translational Jacobian matrix relating the joint velocity vector $\dot{\mathbf{q}} = [\dot{q}_1, \dot{q}_2, \dot{q}_3]^T$ to the fingertip linear velocity $\dot{\mathbf{p}}_{tip} = [\dot{x}_{tip}, \dot{y}_{tip}, \dot{z}_{tip}]^T$ is obtained by differentiating Equation (7) with respect to $\mathbf{q}$. Introducing the shorthands $\rho \equiv L_2 + L_3 \cos q_2 + L_4 \cos(q_2 + q_3)$ for the in-plane radial reach from the MCP joint, $\sigma \equiv L_3 \sin q_2 + L_4 \sin(q_2 + q_3)$, and $s_{23} \equiv \sin(q_2 + q_3)$, $c_{23} \equiv \cos(q_2 + q_3)$, the Jacobian takes the form

$$\mathbf{J}(\mathbf{q}) = \frac{\partial \mathbf{p}_{tip}}{\partial \mathbf{q}} = \begin{bmatrix} -\rho \sin q_1 & -\sigma \cos q_1 & -L_4 s_{23} \cos q_1 \\ \rho \cos q_1 & -\sigma \sin q_1 & -L_4 s_{23} \sin q_1 \\ 0 & L_3 \cos q_2 + L_4 c_{23} & L_4 c_{23} \end{bmatrix} \tag{8}$$

Each column has a clear geometric interpretation: the first column represents the contribution of the MCP joint (q_1), which rotates the finger plane about the palm normal and therefore produces no vertical motion; the second and third columns represent the in-plane contributions of the PIP and DIP joints (q_2, q_3), expressed in the palm-base frame through the rotation by q_1.

2.3.3. Inverse Kinematics

Since each finger has three actuated DoF matching the three task-space coordinates $(x_{tip}, y_{tip}, z_{tip})$, the inverse problem admits a unique physically realizable solution within the joint limits, without any redundancy. The closed-form solution is obtained by decoupling the MCP rotation from the planar motion of the PIP and DIP joints, which reduces the three-dimensional inverse problem to a one-dimensional azimuthal projection followed by a planar two-link (2R) inverse-kinematics problem in the resulting finger plane.

Because the MCP joint axis is perpendicular to the palm plane, the MCP angle q_1 is determined directly from the horizontal projection of the fingertip onto the palm plane as

$$q_1 = \operatorname{atan2}\left(y_{\text{tip}},\ x_{\text{tip}} - L_1\right). \tag{9}$$

Once q_1 is known, the fingertip position is expressed in the resulting finger plane through the radial coordinate r, measured from the PIP joint, and the vertical coordinate z:

$$r = \sqrt{(x_{tip} - L_1)^2 + y_{tip}^2} - L_2, \qquad z = z_{tip}. \tag{10}$$

The remaining sub-problem is a standard planar 2R inverse kinematics in the (r, z) plane with link lengths L_3 and L_4, whose closed-form solution is

$$q_3 = \operatorname{atan2}\left(\pm\sqrt{1 - D^2},\ D\right), \qquad D = \frac{r^2 + z^2 - L_3^2 - L_4^2}{2 L_3 L_4}, \tag{11}$$

$$q_2 = \operatorname{atan2}(z,\ r) - \operatorname{atan2}(L_4 \sin q_3,\ L_3 + L_4 \cos q_3). \tag{12}$$

The sign of the square root in Equation (11) selects between the two geometric branches (elbow-up and elbow-down); the joint range $q_3 \in [0^\circ, 90^\circ]$ specified for the KISP Hand uniquely selects the positive branch, ensuring a single physically realizable solution. The reachability condition $|D| \leq 1$ delimits the task-space region accessible to a single finger, which is consistent with the workspace boundary characterized numerically in Section 3.

2.4. Control Method Based on Advanced Blind Grasping

2.4.1. Theoretical Background

In orbital environments, capturing uncooperative objects or space debris presents significant challenges due to dynamic uncertainties and limited sensor reliability. To ensure

operational robustness under these conditions, the proposed KISP Hand is designed as a sensorless system, intentionally excluding tactile sensors from its fingertips. This design choice is consistent with the centralized shielding strategy introduced in Section 2.1, in which only purely mechanical elements—links and tendons—are exposed to the external space environment, while all electronic components remain enclosed within the shielded palm housing.

However, achieving stable grasping without real-time sensory feedback poses a substantial technical hurdle, as the precise contact state and object geometry remain unknown. To overcome these constraints, this study adopts an advanced blind grasping method based on a groping strategy, which relies solely on the real-time geometric information of the finger positions without prior knowledge of the object's shape, mass, or center of mass [31]. A virtual groped shape is defined by connecting the contact spots P_i of each fingertip. For N contact points, the geometric centroid C_g is calculated as the arithmetic mean of the fingertip positions:

$$C_g = \frac{1}{N}\sum_{i=1}^{N} P_i \tag{13}$$

To ensure a stable grasp, the nominal contact force direction $\hat{f}_i$ for each finger is directed from P_i toward C_g:

$$\hat{f}_i = \frac{C_g - P_i}{\|C_g - P_i\|} \tag{14}$$

The magnitude of the contact force α_i must satisfy the force equilibrium condition $\sum \alpha_i \hat{f}_i = 0$. To enhance robustness against disturbances, the force distribution is designed to be inversely proportional to the distance between the contact spot and the centroid:

$$\alpha_2 = \frac{\|C_g - P_1\|}{\|C_g - P_2\|}\alpha_1 \tag{15}$$

The parameter α_1 is defined as a user-specified grasping force, while the remaining magnitudes are obtained from the equilibrium equations.

2.4.2. Implementation for Tendon-Driven System

The control system of the KISP Hand implements the proposed grasping strategy in a real-time framework for tendon-driven mechanisms. At each control cycle with $DT = 0.01$ s, the controller samples the motor encoder data m_i, computes the corresponding joint angles q_i and fingertip positions P_i, and updates the centroid C_g.

The controller then defines the contact force vectors f_i to converge toward C_g and maps them into joint space using the transpose of the Jacobian matrix J_i^T, following the principle of virtual work:

$$\tau_i = \alpha_i J_i^T \hat{f}_i \tag{16}$$

Equation (16) represents the ideal joint-space quantity corresponding to the desired fingertip force distribution. However, in the tendon-driven KISP Hand, the controller cannot directly apply this quantity as a physical joint torque, since actuation occurs through motor-level commands. Accordingly, we reformulate the control input as a duty-cycle command proportional to the desired joint velocity:

$$u_i = \tau_i + k_i \Delta q_i \tag{17}$$

The spring stiffness coefficient k_i provides a restoring force based on the joint displacement, thereby enhancing stability and facilitating convergence during grasp acquisition. The value of k_i is physically realized by the passive torsion springs installed at the inter-

mediate and distal joints of each finger, whose stiffness values are specified in Table 2 (3.81 N·mm/deg and 1.88 N·mm/deg, respectively). In implementation, the controller bounds u_i and converts it into motor-level duty commands, enabling practical execution under the constraints of the tendon-driven mechanism. Figure 5B illustrates the decision-making process for selecting the grasping mode.

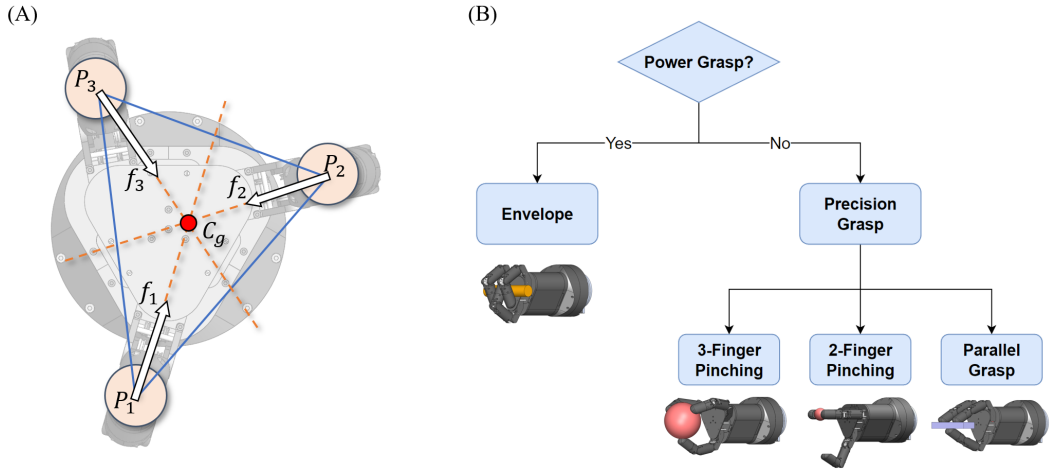


Figure 5. Implementation of the blind grasping strategy: Force distribution toward C_g (**A**), Grasp mode selection flowchart (**B**).

2.5. Electronics

The electronic and control system of the proposed gripper was designed with a primary focus on the rapid functional validation of the EM. The specifications of the key electronic components comprising the control system are listed in Table 4, and the physical layout and photographs of the control boards are presented in Figure 6A. As illustrated, the control boards are safely enclosed within an aluminum shell for cosmic radiation shielding and are integrated with the aforementioned routing structure designed to minimize cable friction. As further depicted in Figure 6A, the fabricated control board currently utilizes a dual-layer structure. However, in anticipation of the volumetric increase of individual components upon transition to space-grade alternatives, the internal housing was designed with sufficient clearance to accommodate up to a four-layer stacked configuration.

Table 4. Main Electronic Components of the EM.

Component	Functional Description
STM32G474RETx	Main MCU for system control and motor command processing.
TCAN332GDCNx	CAN transceiver for communication with the high-level controller.
DRV8845	Integrated motor driver for actuator control.
MP9943A, LM1086	Voltage regulators for stable power distribution across the system.
DCX 22S + ENX10	DC motor and encoder assembly for joint actuation.

Given the characteristics of the EM phase in standard space systems [32,33], the current control system is constructed using commercial off-the-shelf (COTS) components. Specifically, an STMicroelectronics microcontroller unit (MCU) was selected as the main controller to facilitate development efficiency. However, the control architecture depicted in Figure 6B is highly portable and hardware-agnostic, ensuring that the control logic can be easily migrated and executed even if the MCU is replaced with a space-grade alternative.

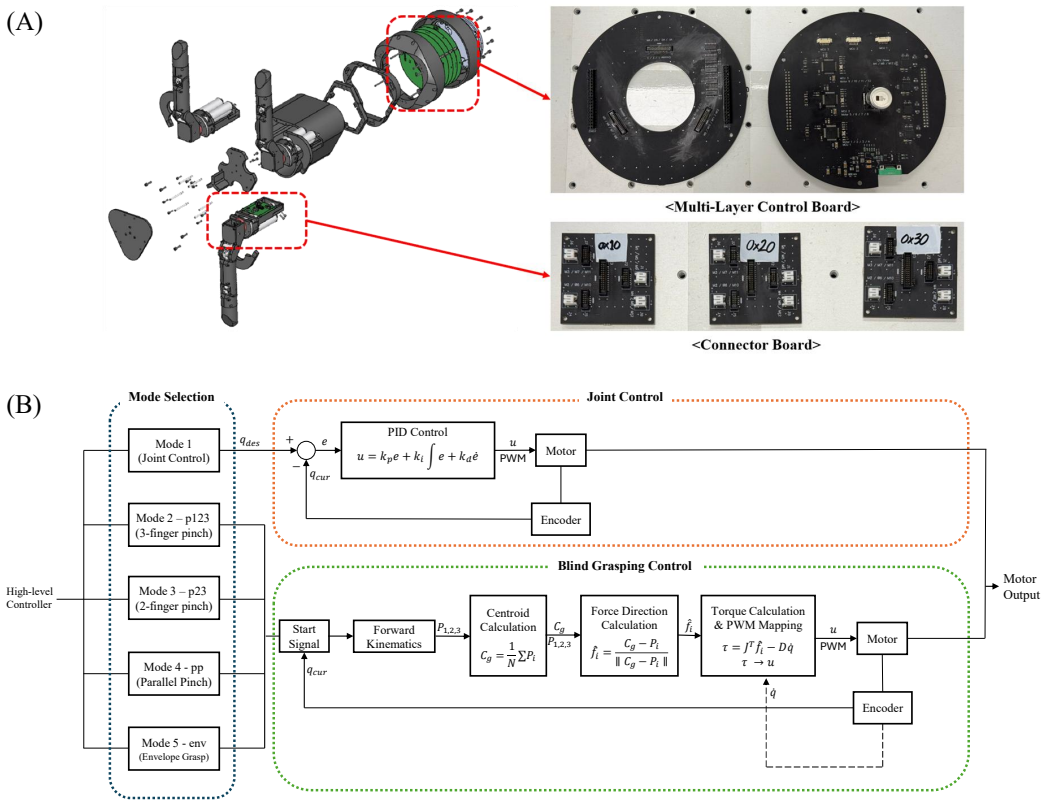


Figure 6. View of the KISP Hand illustrating the physical arrangement of the custom control boards (**A**), block diagram of the control architecture implemented on the board (**B**).

The remaining electronic components were also strategically selected from manufacturers that offer space-qualified equivalents with identical specifications, anticipating the future transition to an EQM. Detailed plans for component replacement and system upgrades for space environment qualification will be discussed in Section 5.3, Future Work.

3. Performance Analysis

3.1. Workspace & Manipulability Analysis

In this section, the kinematic performance of the KISP Hand is numerically characterized in terms of workspace volume and manipulability. Because the corresponding indices are not consistently reported across prior space-qualified grippers (see Table 1), the analysis presented here focuses on a self-contained quantification of the kinematic trade-off resulting from the transition to a 9-DoF symmetric three-finger configuration, complementing the design-space positioning provided in Table 1.

The workspace volume was estimated using a Monte Carlo sampling approach combined with a voxel-grid discretization method [34]. Joint configurations were randomly sampled within the predefined joint limits, and the corresponding fingertip positions were computed via forward kinematics. The resulting point cloud was then discretized into a uniform three-dimensional grid of resolution N_{grid}, where the bounding box of the point cloud was evenly divided into N_{grid}^3 voxels.

A voxel is considered occupied if at least one sampled point falls within it, and the workspace volume is estimated as:

$$V = N_{\text{occ}} \cdot \frac{(x_{\max} - x_{\min})(y_{\max} - y_{\min})(z_{\max} - z_{\min})}{N_{grid}^3} \tag{18}$$

N_{occ} denotes the number of occupied voxels.

The union workspace of all three fingers was obtained by merging the per-finger voxel sets and eliminating duplicate voxels, while the common workspace was defined as the intersection of all three finger voxel sets.

As shown in Figure 7 and Table 5, the total reachable volume of the union workspace is $1.308 \times 10^{-2}\,\mathrm{m}^3$, while the common three-finger workspace (shared between three fingers) is $1.34 \times 10^{-4}\,\mathrm{m}^3$.

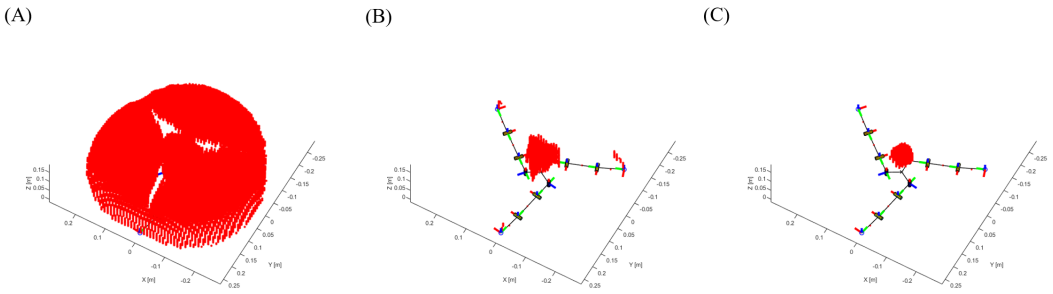


Figure 7. Workspace of KISP Hand: Total reachable workspace of all fingers (**A**), Common workspace shared between all three fingers (**B**), Three-finger common workspace for grasping tasks (**C**).

Table 5. Kinematic Performance Indices of the KISP Hand.

Category	Index	Value
Workspace	Total Union Volume	$1.308 \times 10^{-2}\,\mathrm{m}^3$
	Common Volume	$5.54 \times 10^{-4}\,\mathrm{m}^3$
	Common Volume (Shared between three fingers)	$1.34 \times 10^{-4}\,\mathrm{m}^3$
Manipulability	Max (normalized)	1.000
	Mean (normalized)	0.516
	Min (normalized)	3.0×10^{-4}

The manipulability index was evaluated using Yoshikawa's measure [35], defined as $M = \sqrt{\det(J(q)J(q)^T)}$, where $J(q) \in \mathbb{R}^{3\times n}$ is the translational Jacobian at the fingertip frame. Joint configurations were drawn via the same Monte Carlo sampling procedure described above, and the resulting scalar field was spatially averaged within each occupied voxel to yield a position-resolved manipulability map. The reported indices are normalized by the maximum value observed across all voxels, such that the normalized index $\bar{M}$ is defined as:

$$\bar{M} = \frac{M}{M_{\max}} = \frac{\sqrt{\det(J(q)J(q)^T)}}{\max \sqrt{\det(J(q)J(q)^T)}} \tag{19}$$

The mean normalized index of 0.516 indicates that the gripper operates far from singular configurations across the majority of its workspace, as visualized in Figure 8. The minimum value of 3.0×10^{-4} reflects singular boundaries at the workspace extremes; in practice, however, such configurations lie outside the contact-driven envelope of the blind grasping strategy, in which finger motion converges toward the geometric centroid C_g (Section 2.4) and therefore does not approach the kinematic boundaries.

3.2. Radiation Shielding Analysis

This subsection presents a GEANT4-based [36] Monte Carlo radiation transport analysis conducted to quantitatively assess the shielding performance of the proposed 4 mm aluminum cavity design. As stated in Section 2.1, the 4 mm aluminum thickness was adopted as a literature-grounded baseline informed by prior analytical studies on aluminum attenuation in LEO/GEO environments [23–27]. The purpose of this subsection is to quantify, at the EM stage, the shielding behavior of the adopted thickness under the

as-built cavity geometry and to identify reinforcement requirements for the subsequent EQM phase.

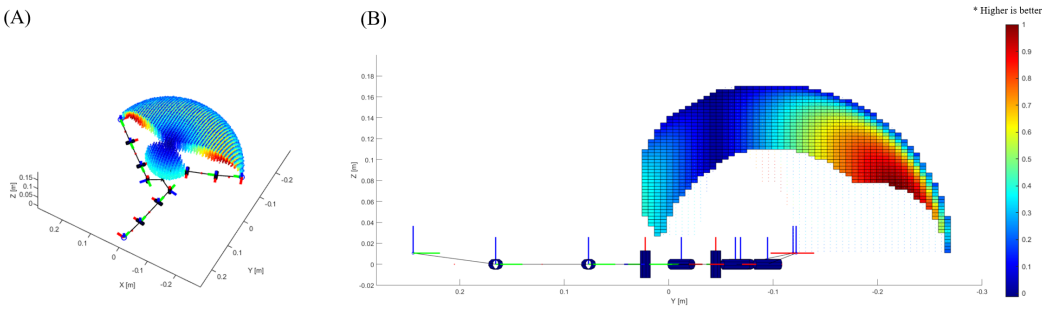


Figure 8. Manipulability analysis of KISP Hand's finger module: 3D view of manipulability distribution over the workspace (**A**), Cross-sectional view on the X-plane (**B**).

The simulation was performed using the Shielding physics list of GEANT4 version 11.4. The as-built CAD geometry of the KISP Hand was imported as STL tessellated solids representing a 16-part assembly, and two silicon sensitive volumes of $10 \times 10 \times 1\,\mathrm{mm}^3$ were placed at (i) the Upper Cavity, located at $(0, -60, 0)$ mm and housing the motor drivers and actuator board, and (ii) the Lower Cavity, located at $(0, -220, 0)$ mm and housing the main control board and connector board. Primary electrons were sampled from the AE-8 MAX trapped-electron spectrum [37] (0.04–7 MeV, integral flux $4.16 \times 10^7\,\mathrm{cm}^{-2}\,\mathrm{s}^{-1}$) derived from SPENVIS [38,39] under a 5-year GEO mission profile, and emitted from a 400-mm-radius spherical surface centered on the assembly with a cosine-law angular distribution. The manipulator-side connector region was modeled as fully shielded, while all other directions were treated as a 4π isotropic source. Each case was simulated with 10^9 primary electrons.

Three configurations were compared to quantitatively assess the shielding performance:

- 4 mm Al sphere: the center-point dose of an idealized 4 mm aluminum spherical shell computed using SPENVIS SHIELDOSE-2 [40] under the same mission profile (862 Gy = 86.2 krad). This serves as the planar-assumption reference for the 4 mm aluminum thickness adopted in this work.
- No housing: the sensors placed in vacuum without any shielding structure, providing the unshielded dose ground truth.
- KISP Hand: the actual as-built EM geometry developed in this work, including the cable-access opening and cover-plate gaps introduced for ground-test mass reduction.

The resulting 5-year cumulative GEO doses are summarized in Table 6 (the raw GEANT4 simulation logs and the corresponding SPENVIS environment data are provided in the Supplementary Materials, Dataset S4). Relative to the no-housing baseline, the KISP Hand achieves shielding factors of 75× (98.7 %) at the Upper Cavity and 1260× (99.9 %) at the Lower Cavity, indicating that the 4 mm aluminum housing provides quantitatively substantial attenuation at the cavity-internal locations.

Table 6. 5-year GEO cumulative dose at electronic-component locations.

Configuration	Upper Cavity [krad]	Lower Cavity [krad]	Attenuation (Upper)	Attenuation (Lower)
4 mm Al sphere	86.2	86.2	—	—
No housing	$20{,}053 \pm 82$	$20{,}126 \pm 82$	—	—
KISP Hand	268.6 ± 9.2	15.9 ± 2.5	98.7 % (75×)	99.9 % (1260×)

Comparison with the SHIELDOSE-2 planar reference (86.2 krad) reveals a spatially dependent shielding profile within the cavity. The Lower Cavity dose (15.9 ± 2.5 krad) falls below the planar reference at 0.18×, reflecting the additional shielding provided by the surrounding assembly mass at the deeper internal location. In contrast, the Upper Cavity (268.6 ± 9.2 krad) exceeds the planar reference by 3.1×, indicating localized shielding non-uniformities concentrated in this region. These non-uniformities are attributable to (i) thin regions intentionally introduced for ground-test mass reduction, (ii) cable interfaces, cover-plate gaps, and structural openings, and (iii) unfilled bolt holes (to be filled with aluminum fasteners in EQM/FM). The present analysis thus constitutes a conservative evaluation in which all such weak regions are treated as fully exposed; these regions are identified as targets for reinforcement at the EQM stage (Section 5.3).

In absolute terms, the Upper Cavity dose remains comparable to or above the typical total-ionizing-dose tolerance of space-grade electronic components, indicating that additional reinforcement beyond the present 4 mm aluminum baseline—such as a graded-Z inner liner—will be required at the EQM stage (Section 5.3).

In summary, the results provide a quantitative assessment of the attenuation behavior of the 4 mm aluminum baseline adopted in Section 2.1 at the EM stage, while concurrently indicating that EQM-phase reinforcement is required to satisfy component-level radiation-tolerance requirements.

4. Experiments

This section presents the functional validation experiments and corresponding results for the proposed KISP Hand EM. Building upon the mechanical design and kinematic analyses presented in Sections 2 and 3, this section empirically verifies the practical effectiveness of the proposed hardware and control strategies under representative operating conditions.

The KISP Hand achieves independent multi-joint mobility through a tendon-driven mechanism combined with a passive restoration system, as described in Section 2.2. To reduce the number of radiation-sensitive components exposed to the space environment, the system adopts a sensorless architecture that relies solely on motor encoders. The consequent absence of direct position feedback at the fingertips is addressed through the advanced blind grasping strategy, which estimates contact geometry from encoder data alone.

To demonstrate the operational feasibility of the proposed system for OOS missions, two sequential experiments were conducted:

- Mechanical Reliability Verification: The repeatability of the tendon-driven finger joints was quantitatively evaluated across 50 repeated trials, following an ISO 9283–inspired protocol [41] adapted to the sensorless architecture of the KISP Hand: the repeatability is defined with respect to the encoder-referenced mean arrival position rather than the commanded reference, thereby isolating the mechanical consistency of the structure from controller-dependent tracking accuracy. The implications and limitations of this adaptation are discussed at the end of Section 4.1.
- Grasping Demonstration: The robust grasping stability for both structured and unstructured objects was validated using the advanced blind grasping methodology, demonstrating its high adaptability to the irregular targets and uncertain environments typically encountered in OOS scenarios.

4.1. Mechanical Reliability: Repeatability Verification

In this study, experiments following an ISO 9283 [41]—inspired protocol, adapted to the sensorless flight configuration as described above, were conducted to verify the mechanical repeatability of the developed robotic hand.

In the Recording Phase, a specific joint is driven to a target angle according to the user's command, and the actual trajectory reached (q_{actual}) is recorded via encoders. Subsequently, in the Playback Phase, the recorded trajectory is set as the reference input (q_{ref}), and the same motion is repeated 50 times ($n = 50$) using a PID controller. The arrival errors at the peak and valley of each cycle were collected to calculate the standard deviation (σ).

The 100 Hz sampling rate ($\Delta T = 0.01$ s) was selected to provide sufficient bandwidth relative to the mechanical response of the tendon-driven finger joints, and the empirically tuned gains listed in Table 7 yielded stable closed-loop tracking with no observable oscillation across all 50 trajectory playback cycles (Figures 9 and 10).

Table 7. PID gains used in the repeatability experiments of Section 4.1. The joint-control law is $u = k_p\, e + k_i \int e\, dt - k_d\, \dot{q}$, where $e = q_{\text{ref}} - q$ and $\dot{q}$ denotes the measured joint velocity, sampled at $\Delta T = 0.01$ s. Gains were empirically tuned per joint type.

Joint Type	k_p	k_i	k_d
MCP	0.45	0.20	0.04
PIP	0.65	0.12	0.05
DIP	0.25	0.10	0.03

Based on these measurements, the Repeatability (RP) was defined as $\pm 3\sigma$ to represent the positioning consistency. Furthermore, the RP/ROM ratio was calculated to evaluate the precision relative to the total Range of Motion (ROM), where a lower percentage indicates higher movement consistency across the entire operational space.

Individual tests were performed for the flexion/extension of the MCP (Joints 0, 3, 6), PIP (Joints 1, 4, 7), and DIP (Joints 2, 5, 8) joints (See Figure 9A–C). Additionally, a simultaneous independent control test of the PIP and DIP joints was conducted to verify the validity of the decoupling formulation and the resulting control stability during actual grasping (See Figure 9D). This is because, as detailed in Section 2.2, the PIP and DIP joints are structurally configured such that they mechanically influence each other.

Figure 10A–C show the time-response curves during single-joint actuation for each joint group, while Figure 10D illustrates the simultaneous actuation characteristics of the PIP and DIP joints. In all plots, the actual trajectories of the 50 repeated cycles overlap so closely that they appear as a single line, indicating that the mechanical rigidity of the hardware and the software control algorithm work in harmony.

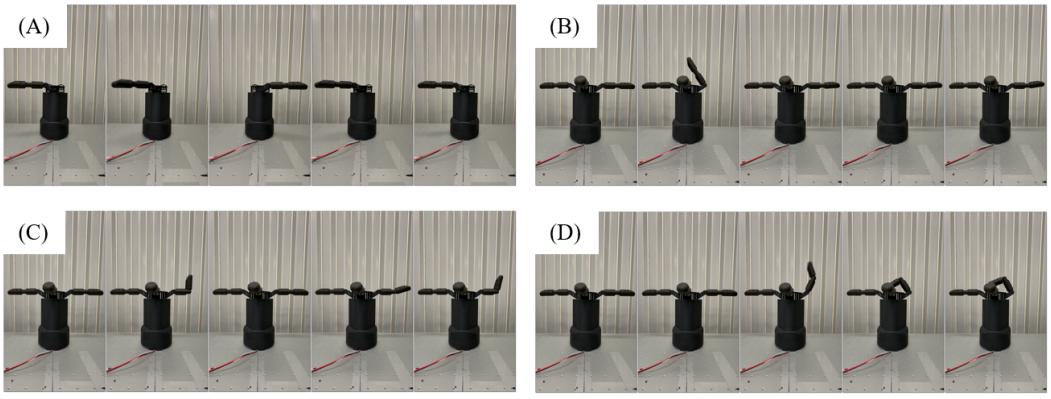


Figure 9. Sequential snapshots of one forward–return cycle for each joint repeatability test: MCP joint flexion/extension (**A**), PIP joint flexion/extension (**B**), DIP joint flexion/extension (**C**), and simultaneous independent control of PIP and DIP joints, verifying that each joint maintains its repeatability under multi-joint actuation (**D**).

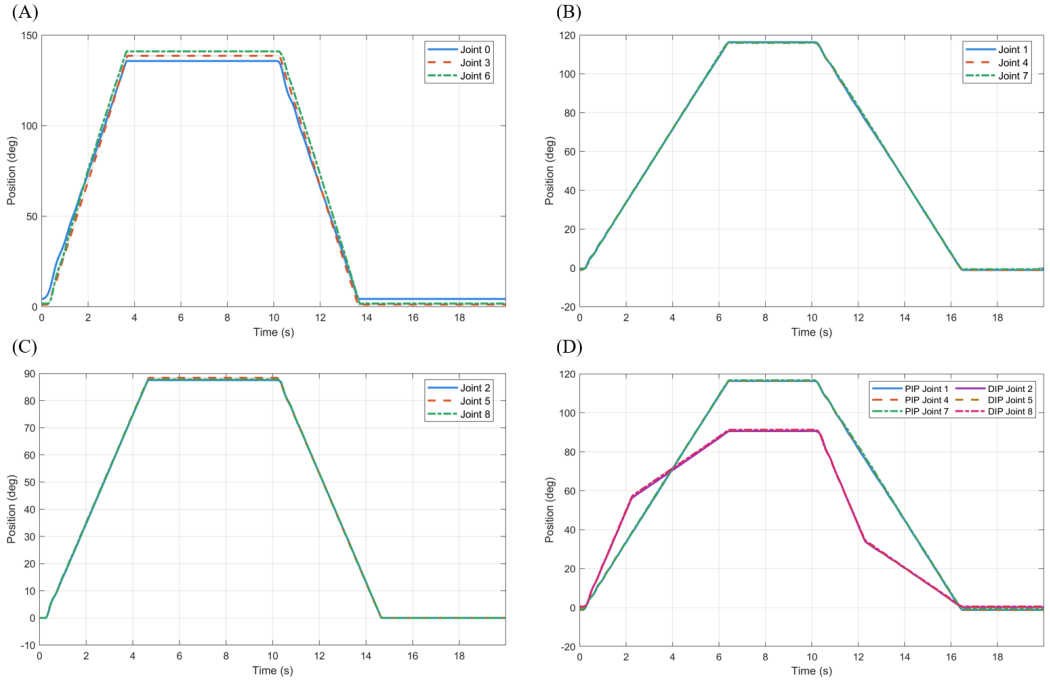


Figure 10. Time-response trajectories of finger joints during the repeatability verification cycles: MCP joints (Joint 0, 3, 6) flexion/extension (**A**), PIP joints (Joint 1, 4, 7) flexion/extension (**B**), DIP joints (Joint 2, 5, 8) flexion/extension (**C**), and Simultaneous independent control of PIP and DIP joints to verify multi-joint actuation stability (**D**).

Table 8 provides a statistical summary of the data obtained from the 50 repetitions (the complete raw measurement data are provided in the Supplementary Materials, Dataset S1). The MCP joints exhibited a maximum repeatability within $\pm 0.4947^\circ$, with an error rate relative to the range of motion (RP/ROM) measured at 0.355% or less. The PIP joints showed high precision with RP values ranging from $\pm 0.0769^\circ$ to $\pm 0.2067^\circ$, and the DIP joints ranged from $\pm 0.0853^\circ$ to $\pm 0.149^\circ$. Notably, even in the simultaneous actuation environment (PD mode), the system maintained a precision level ($\pm 0.0467^\circ$ to $\pm 0.1639^\circ$) comparable to that of single-joint actuation, indicating that mechanical backlash is effectively suppressed and the control algorithm operates stably.

Consequently, the developed robotic hand demonstrated high mechanical reliability suitable for precision object manipulation and repetitive tasks. To further substantiate the comparative repeatability of the three joint groups, a non-parametric inferential analysis was conducted on the normalized arrival deviations. For each of the 300 trial outcomes per group (3 joints $\times$ 50 trials $\times$ peak/valley arrivals), the absolute deviation from the corresponding group mean was normalized by the joint ROM and expressed in percent. Because Shapiro–Wilk tests indicated significant departures from normality in all three groups ($p < 0.001$), the Kruskal–Wallis H-test [42] was selected over one-way ANOVA. The test revealed a statistically significant difference among the MCP, PIP, and DIP groups ($H(2) = 90.96$, $p < 0.001$), with an epsilon-squared effect size of $\varepsilon^2 = 0.101$ indicating a medium-magnitude separation between groups.

Post-hoc pairwise comparisons using Dunn's test with Bonferroni correction [43] showed that MCP differs significantly from both PIP and DIP ($p < 0.001$ in both cases), whereas the PIP and DIP groups were statistically indistinguishable ($p = 0.099$). The slightly larger MCP dispersion is consistent with its role as the longest-throw joint (ROM = 140°) operating under direct loading from the distal phalanges, while the statistical equivalence of PIP and DIP indicates that the tendon coupling formulation derived

in Section 2.2 does not introduce additional positional variability at the distal joint. The full distribution is summarized in Figure 11.

Table 8. Repeatability summary of all finger joints (RP = $\pm 3\sigma$, $n = 50$).

Group	Joint	Peak Arrival			Valley Arrival		
		σ [deg]	RP [deg]	RP/ROM [%]	σ [deg]	RP [deg]	RP/ROM [%]
MCP	Joint 0	0.0682	±0.2046	0.151	0.0775	±0.2324	0.171
	Joint 3	0.0952	±0.2855	0.206	0.0570	±0.1710	0.123
	Joint 6	0.1116	±0.3348	0.240	0.1649	±0.4947	0.355
PIP	Joint 1	0.0331	±0.0994	0.084	0.0689	±0.2067	0.174
	Joint 4	0.0283	±0.0850	0.072	0.0306	±0.0919	0.078
	Joint 7	0.0328	±0.0984	0.083	0.0256	±0.0769	0.065
DIP	Joint 2	0.0284	±0.0853	0.096	0.0314	±0.0943	0.106
	Joint 5	0.0303	±0.0910	0.102	0.0389	±0.1166	0.131
	Joint 8	0.0350	±0.1050	0.118	0.0440	±0.1320	0.149
PD – PIP	Joint 1	0.0297	±0.0891	0.075	0.0546	±0.1639	0.138
	Joint 4	0.0408	±0.1225	0.103	0.0505	±0.1516	0.127
	Joint 7	0.0397	±0.1190	0.100	0.0354	±0.1063	0.089
PD – DIP	Joint 2	0.0156	±0.0467	0.051	0.0371	±0.1114	0.123
	Joint 5	0.0316	±0.0948	0.104	0.0520	±0.1561	0.171
	Joint 8	0.0394	±0.1183	0.130	0.0250	±0.0749	0.082

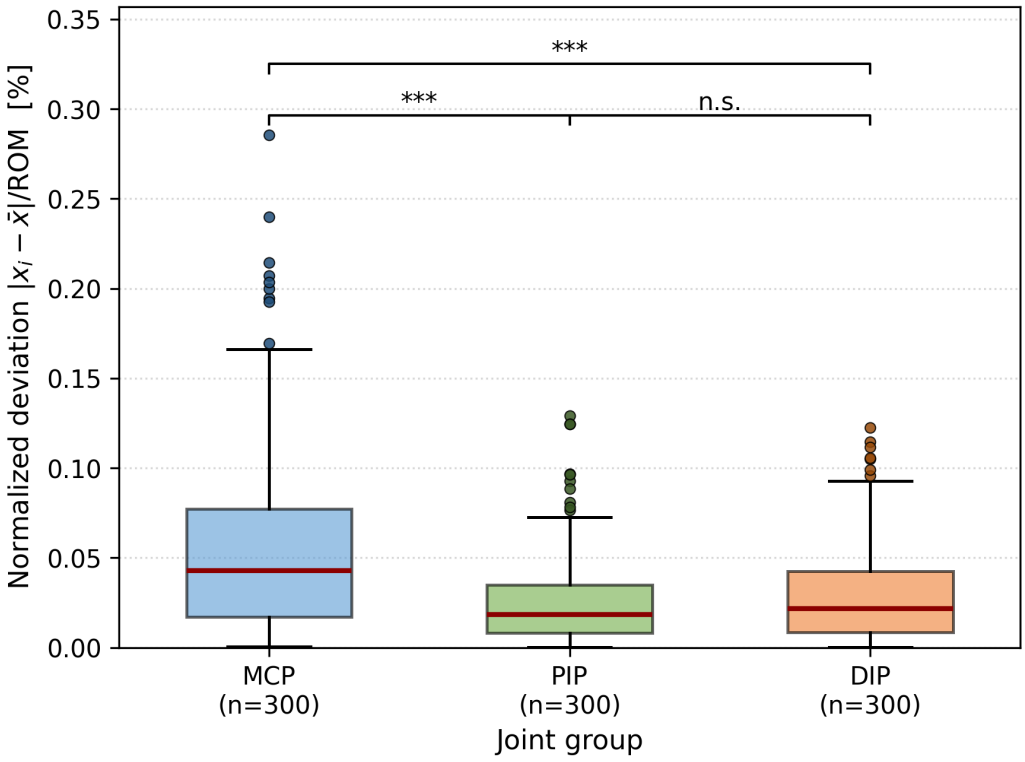


Figure 11. Distribution of normalized arrival deviations $|x_i - \bar{x}|$/ROM for the three joint groups ($n = 300$ each, combining peak and valley arrivals across 50 trials and three joints per group). Boxes indicate the interquartile range, red lines indicate medians, and colored dots indicate outliers beyond 1.5 × IQR. Significance brackets are based on Dunn's test with Bonferroni correction (***: $p < 0.001$; n.s.: not significant).

We note that the repeatability metric reported here characterizes the mechanical and control consistency of the as-designed sensorless architecture relative to its own encoder reference, rather than absolute fingertip accuracy with respect to an external ground truth. The latter requires joint-side instrumentation that the present flight configuration

intentionally omits for radiation-tolerance reasons (see Section 2), and is therefore deferred to the EQM-phase verification campaign described in Section 5.3.

4.2. Grasping Demonstration

To verify the practical utility and mechanical adaptability of the proposed KISP Hand, a series of grasping tests was conducted using objects of various shapes and sizes. The evaluation was designed to demonstrate the hand's ability to achieve stable grasping through the advanced blind grasping methodology across all four grasping modes supported by the design.

Figure 12 illustrates the grasping sequences for four representative scenarios. In (A), the hand performs a power grasp. In contrast, (B), (C), and (D) demonstrate different Precision Grasp configurations. Specifically, (B) shows a parallel grasp, (C) presents a two-finger pinching configuration, and (D) illustrates a three-finger pinching configuration. Notably, the coordinated motion of multiple fingers in (D) highlights the hand's capability for fine and adaptive manipulation.

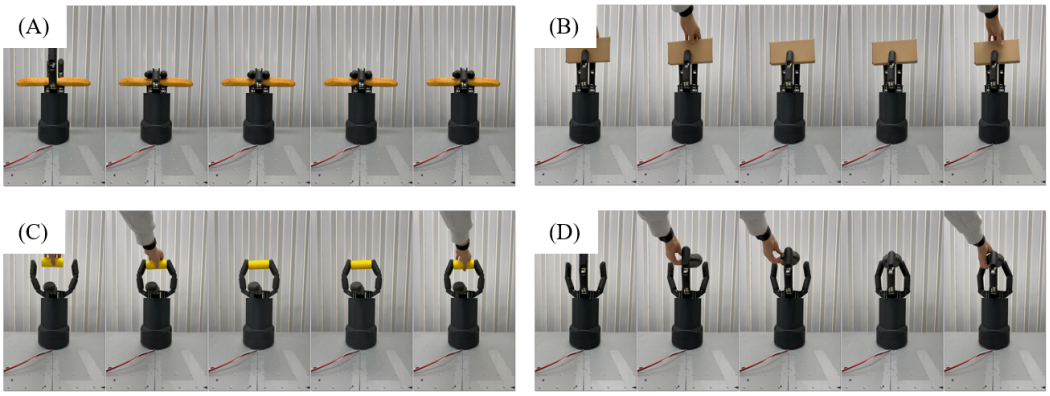


Figure 12. Sequential snapshots of the grasping demonstrations across four distinct scenarios: power grasp (**A**), parallel grasp (**B**), 2-finger pinching (**C**), and 3-finger pinching (**D**).

The objects used in each demonstration scenario, along with their nominal dimensions and masses, are summarized in Table 9. To quantify grasping reliability, each (mode, object) combination was tested over 10 trials, yielding 160 trials in total; the resulting success rates are summarized in Table 10 (the per-trial measurement data are provided in the Supplementary Materials, Datasets S2 and S3). The power grasp achieved 100% success across all objects, while the Precision Grasp modes ranged from 82.5% to 92.5%. The lowest per-cell rate was observed for the cylindrical object under parallel grasp (5/10), where the limited tangential friction at the fingertip surfaces was insufficient to prevent slippage; this is identified as a specific improvement target for the EQM revision.

Table 9. Test object specifications for grasping evaluation. Four objects spanning representative shape categories were used across all four grasping modes.

ID	Object	Dimensions [mm]	Mass [g]
obj1	Baguette-shaped model	70 × 420 × 40	33
obj2	Small cardboard box	120 × 240 × 30	55
obj3	Small plastic cylinder model	∅50 × 120	36
obj4	Stone-shaped model	100 × 150 × 40	16

Table 10. Grasping success rate across four modes and four objects.

Mode	obj1	obj2	obj3	obj4	Total
Power Grasp	10/10 (100%)	10/10 (100%)	10/10 (100%)	10/10 (100%)	40/40 (100.0%)
Parallel Grasp	9/10 (90%)	9/10 (90%)	5/10 (50%)	10/10 (100%)	33/40 (82.5%)
2-Finger Pinching	8/10 (80%)	10/10 (100%)	9/10 (90%)	10/10 (100%)	37/40 (92.5%)
3-Finger Pinching	7/10 (70%)	9/10 (90%)	10/10 (100%)	10/10 (100%)	36/40 (90.0%)

A preliminary disturbance-rejection test was also conducted for the three-finger pinching mode, which exhibits the smallest contact area among the four modes and therefore represents the most challenging condition for sustained grasp stability. Using obj4 (Table 9), lateral perturbations were applied manually by an operator after the grasp had settled ($t > 1.5$ s) in each of 10 trials; perturbation magnitudes were not instrumented in this preliminary assessment and were intentionally varied across trials.

Calibrated perturbation testing with an instrumented loading apparatus is planned for the EQM verification campaign (Section 5.3). Despite the uncalibrated input, the post-disturbance response was fully captured through high-rate motion logging. The grasp was retained in all 10 trials (Table 11), with a steady-state lateral RMS displacement of 3.61 mm (max 4.98 mm) and a systematic vertical drift of -0.73 mm along the gravity direction (max -1.11 mm), as summarized in Table 12. The consistent sign of the vertical drift indicates a small but systematic slippage under gravity, consistent with the friction-limited behavior observed under parallel grasps.

Table 11. Disturbance-rejection holding success rate for the 3-finger pinching mode.

Object	Trials	Success	Rate
obj4 (3-finger pinching)	10	10	100%

Table 12. Object position drift in the post-settling steady state (t > 1.5 s) following disturbance. cgxy denotes lateral displacement in the grasp plane; cgz denotes vertical drift.

Trial	cgxy_max [mm]	cgxy_RMS [mm]	cgz_drift [mm]	cgz_RMS [mm]
t01	4.10	3.77	−1.11	1.20
t02	3.37	3.33	−0.82	0.85
t03	2.55	2.24	−0.73	0.81
t04	3.65	2.95	−0.60	0.65
t05	3.41	2.99	−0.88	0.96
t06	4.29	4.15	−1.01	1.07
t07	4.98	4.74	−0.60	0.70
t08	4.11	3.92	−0.41	0.52
t09	4.31	3.91	−0.60	0.69
t10	4.25	4.14	−0.51	0.53
Mean	3.90	3.61	−0.73	0.80
Max	4.98	—	−1.11	1.20

These results demonstrate that the KISP Hand can reliably adapt to objects spanning the geometric diversity expected in OOS target sets and achieve stable grasping under the kinematic and contact-state uncertainties addressed by the blind grasping strategy, while also identifying fingertip friction as a clear refinement target for subsequent development. Verification under representative space-environment conditions (thermal-vacuum, radiation, microgravity dynamics) is outside the scope of the present EM study and is deferred to the EQM verification campaign described in Section 5.3.

5. Conclusions

5.1. Summary and Contributions

In this paper, we propose an EM of a multi-joint space gripper named the KISP Hand for OOS missions. The main contributions of this research, which demonstrate the system's performance and feasibility for space missions, are summarized as follows:

- Design Concept and Direction: Proposal of a three-finger, 9-DoF gripper configuration that adopts a design direction widely established in industrial applications and is positioned as a complementary alternative to anthropomorphic high-DoF designs reported in prior space-qualified grippers.
- Radiation Shielding and Hardware Design: Development of a centralized shielding-oriented structural configuration to protect radiation-sensitive internal electronic components, with a 4 mm aluminum specification grounded in prior analytical studies of LEO/GEO aluminum attenuation. The as-built shielding behavior was quantitatively evaluated by GEANT4-based Monte Carlo radiation transport analysis under a 5-year GEO mission profile, yielding cavity-internal shielding factors of 75× and 1260× at the upper and lower cavity locations, respectively, and identifying localized weak regions that constitute reinforcement targets for the subsequent EQM phase.
- Kinematic Performance Characterization: Derivation of the complete single-finger kinematic model including forward kinematics, the Jacobian, and inverse kinematics, as well as numerical verification of the gripper's workspace volume and manipulability distribution.
- Functional Performance Validation: Mechanical repeatability characterization across 50 trials per joint, statistically analyzed via Kruskal–Wallis testing, and grasping demonstrations with quantitative success-rate measurement using the fabricated EM, based on 160 trials across four modes and four objects. Calibrated grasping-force measurement and instrumented disturbance-rejection testing are deferred to the EQM verification campaign.

Through these contributions, this study establishes a design and evaluation basis for three-finger space grippers that complements the anthropomorphic, high-DoF designs reported in prior space-qualified robotic hands.

5.2. Limitations

The limitations identified in this research are summarized as follows:

- Absence of Direct Contact Feedback: To maximize radiation tolerance in space environments, the system adopted a tactile-sensorless architecture that intentionally excludes tactile sensors at the fingertips and relies solely on motor encoders. Consequently, there are limitations in real-time measurement and control of physical interactions, such as contact reaction forces or slip.
- Lack of Thermal Expansion Compensation for Tendon Cables: Although a tendon-driven mechanism is employed, the current system lacks control algorithms or hardware tensioning mechanisms to compensate for the thermal expansion and contraction of the tendon cables caused by extreme temperature variations in space. The UHMWPE fiber used in the current EM exhibits a negative coefficient of linear thermal expansion of -12×10^{-6} K^{-1} [44], which is opposite in sign to that of the aluminum palm housing ($\sim 23 \times 10^{-6}$ K^{-1}) and the PA12 finger housing (~ 80–110×10^{-6} K^{-1}). Under temperature variations, the housing structures and the tendon therefore deform in opposite directions, leading to a non-trivial change in effective tendon length along the routing path. This effect could introduce errors in kinematic precision and variability in grasping force under harsh environmental conditions.

- Environmental Testing Limits of the COTS-based EM: The current system was fabricated at the EM level using COTS components. Although a radiation shielding structure was integrated into the design, direct empirical durability tests under simulated harsh space conditions, such as thermal-vacuum chambers or actual radiation exposure, were outside the scope of this study.

5.3. Future Work

In future work, the current COTS-based EM will be upgraded to an EQM. In terms of mechanical design, the current structural components will be entirely replaced with aluminum components to maximize structural rigidity and radiation shielding performance. Furthermore, the springs used in the joints will be custom-manufactured using space-appropriate materials [45]. To upgrade the control and actuation systems, key electronic components will be replaced with space-qualified parts, such as radiation-hardened MCUs, as outlined in Table 13.

Table 13. Space-qualified components selected for future iterations.

Component	Functional Description
SAMV71Q21RT-DHB-E	Radiation-hardened MCU for high-level communication and motor control.
SN55HVD233-SEP	Space-enhanced CAN transceiver serving as a communication bridge between the MCU and high-level controller.
EPC7012L7C	GaN-based half-bridge converter utilized for motor PWM control and power switching.
TPS7H4010-SEP	Space-grade voltage regulator for precise power supply for motors, encoders, and the MCU.
DCX 22S Space	Space-qualified DC motor for high-reliability joint actuation.

In particular, to address the extreme temperature variations in the space environment, the tendon cables will be replaced with materials exhibiting a lower coefficient of thermal expansion (CTE). Concurrently, advanced control techniques that actively compensate for temperature-induced thermal expansion and contraction will be implemented [46,47].

Following these comprehensive hardware upgrades, functional verification experiments will be conducted under harsh simulated space conditions, including thermal-vacuum (TVAC), vibration, and space radiation environments [48–50]. Through these advancements, this research is expected to contribute to future studies on space grippers and practical OOS missions. In addition, the quantitative analysis presented in Section 3.2 indicates that the 4 mm aluminum shell alone yields cavity-internal doses that remain noticeably higher than the idealized planar reference. This residual excess is partly attributable to secondary radiation (e.g., bremsstrahlung photons) generated within the aluminum shell itself, suggesting that further reduction of the cavity-internal dose cannot be achieved by aluminum thickness increase alone. Accordingly, the EQM iteration will explore graded-Z shielding configurations, in which the aluminum outer shell is complemented by a low-Z inner liner—such as the polyethylene-based spot shielding noted in Section 2.1—to absorb secondary photons generated within the metallic outer layer.

In addition to the environmental qualification experiments described above, the EQM-stage characterization of the KISP Hand will be structured to follow methodological precedents established in prior on-orbit robotic-system evaluation campaigns, such as the Robotics Evaluation and Characterization (REACH) study of the SSRMS [51]. This approach will enable the present ISO 9283-based ground-stage repeatability metrics to be extended into characterization protocols suitable for space-qualified robotic devices, including evaluation under thermal gradients, vacuum conditions, and reduced-gravity dynamics.

Such methodological continuity is essential for translating the ground-based performance verification of the EM into operationally meaningful verification at the qualification stage.

Supplementary Materials: The following supporting information can be downloaded at https://www.mdpi.com/article/10.3390/aerospace13060513/s1: Dataset S1: Joint-level repeatability test data (encoder-referenced joint angles over 50 playback cycles for the MCP, PIP, and DIP joints); Dataset S2: Grasping experiment data (joint angles, contact points, and force vectors for three-finger pinch and envelope grasp modes across multiple objects); Dataset S3: Disturbance test data; Dataset S4: GEANT4 Monte Carlo radiation transport simulation logs (with and without the aluminum housing) and the corresponding SPENVIS space-radiation environment data.

Author Contributions: Conceptualization, T.C.; methodology, T.C.; software, T.C.; validation, T.C.; writing—original draft preparation, T.C.; data curation, T.C.; visualization, T.C.; investigation, T.C.; project administration, D.W., B.-R.S. and D.-H.L.; writing—review and editing, D.W., B.-R.S. and D.-H.L.; funding acquisition, D.W.; supervision, D.-H.L. All authors have read and agreed to the published version of the manuscript.

Funding: This work was supported by the Institute of Civil Military Technology Cooperation, funded by the Defense Acquisition Program Administration and Ministry of Trade, Industry and Energy of the Korean government under Grant 22-CM-EC-36.

Institutional Review Board Statement: Not applicable.

Informed Consent Statement: Not applicable.

Data Availability Statement: The original contributions presented in this study are included in the article. Further inquiries can be directed to the corresponding author.

Acknowledgments: During the preparation of this manuscript, the authors used Gemini 3.1 Pro (Google) for English language editing and grammatical refinement. In addition, a generative AI-based image editing tool was used to enhance the visual quality and compositing of the schematic illustration presented in Figure 1. The authors have carefully reviewed and edited all AI-generated outputs and take full responsibility for the content of this publication.

Conflicts of Interest: The authors declare that this study received funding from the Institute of Civil Military Technology Cooperation, which was funded by the Defense Acquisition Program Administration and the Ministry of Trade, Industry and Energy of the Korean government. The funder had no role in the study design, data collection, data analysis, interpretation of the results, writing of the manuscript, or the decision to publish the article.

Abbreviations

OOS	On-Orbit Servicing
EM	Engineering Model
EQM	Engineering Qualification Model
COTS	Commercial Off-The-Shelf
MCU	Microcontroller Unit
DoF	Degree of Freedom
ROM	Range of Motion
RP	Repeatability
DT	Sampling Time Interval
MCP	Metacarpophalangeal Joint
PIP	Proximal Interphalangeal Joint
DIP	Distal Interphalangeal Joint
LEO	Low Earth Orbit
GEO	Geostationary Orbit

Appendix A. CAD-Based Derivation of the Geometric Coupling Factor k

The geometric coupling factor k in Equation (4) arises from the non-coincident placement of the PIP rotation axis and the grooved bearing center. As the PIP joint rotates, the tendon wraps around the grooved bearing surface to a degree that slightly exceeds the PIP rotation itself, owing to the offset between the two centers.

To quantify this effect, the as-built CAD geometry of the finger module was used to evaluate the tendon path at the two extremes of the PIP range of motion. Figure A1 compares the tendon paths at PIP $= 0^\circ$ (dashed configuration, red tendon) and at PIP $= 120^\circ$ (solid configuration, blue tendon). The wrap-angle change at the grooved bearing center, measured between the two tendon tangent directions, is $\Delta\phi = 123.62^\circ$, which corresponds to a tendon length change of

$$\Delta L = r_b \cdot \Delta\phi = 4.5\text{mm} \cdot \frac{123.62\pi}{180} = 9.71\text{mm} \tag{A1}$$

along the bearing surface. The dimensionless coupling factor is then

$$k = \frac{\Delta\phi}{\Delta q_2} = \frac{123.62^\circ}{120^\circ} \approx 1.03, \tag{A2}$$

which is the value substituted into Equation (4) of the main text.

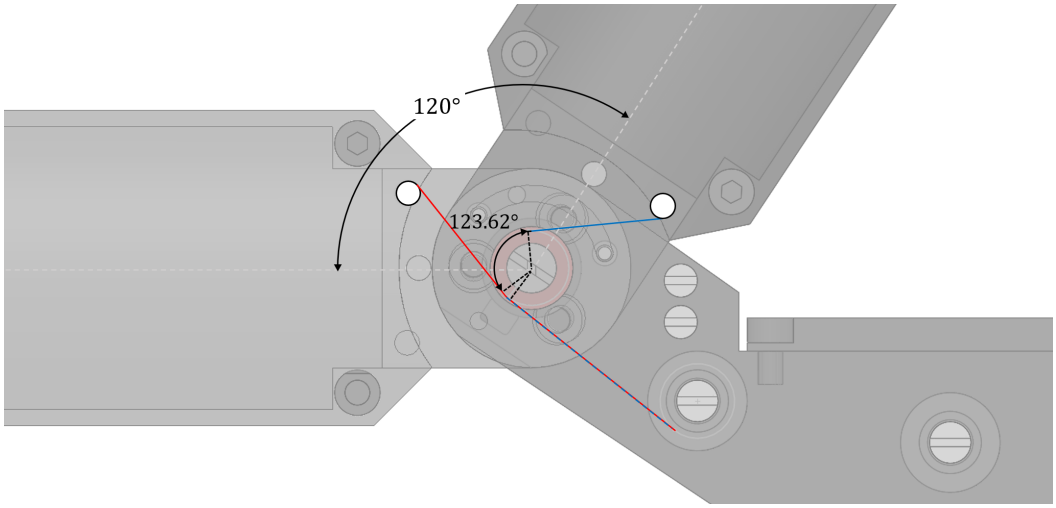


Figure A1. CAD-based derivation of the geometric coupling factor k. The two overlaid finger poses correspond to PIP $= 0^\circ$ (dashed white outline; tendon shown in red) and PIP $= 120^\circ$ (solid grey body; tendon shown in blue). The black arrow indicates the 120° PIP rotation. The change in tendon wrap angle measured at the grooved bearing center is 123.62°, yielding $k = 123.62/120 \approx 1.03$.

References

1. Davis, J.P.; Mayberry, J.P.; Penn, J.P. *On-Orbit Servicing: Inspection, Repair, Refuel, Upgrade, and Assembly of Satellites in Space*; The Aerospace Corporation: El Segundo, CA, USA, 2019.
2. Liou, J.-C. An Active Debris Removal Parametric Study for LEO Environment Remediation. *Adv. Space Res.* **2011**, *47*, 1865–1876. [CrossRef]
3. Papadopoulos, E.; Aghili, F.; Ma, O.; Lampariello, R. Robotic Manipulation and Capture in Space: A Survey. *Front. Robot. AI* **2021**, *8*, 686723. [CrossRef]
4. NASA Office of Inspector General. *NASA's Management of the International Space Station and Efforts to Commercialize Low Earth Orbit*; Report No. IG-22-005; NASA: Washington, DC, USA, 2021.
5. National Academies of Sciences, Engineering, and Medicine. *Review of NASA's Evidence Reports on Human Health Risks*; National Academies Press: Washington, DC, USA, 2016.
6. Nguyen, C.C.; Ngo, H.T.T.; Duong, T.T.C.; Nabili, A. Mechanical Design and Kinematic Analysis of an Autonomous Wrist with DC Motor Actuators for Space Assembly. *Actuators* **2025**, *14*, 542. [CrossRef]

7. Zang, L.; Hou, W.; Liu, L.; Hu, H.; Wang, X.; Jia, Y.; Hao, Y.; Li, Y.; Zhao, B. The Application and Development of Static Pressure Air Floating in the Field of Micro-Low-Gravity Simulation Experiments for Spacecraft. *Lubricants* **2025**, *13*, 258. [CrossRef]
8. Ai, H.; Zhu, A.; Wang, J.; Yu, X.; Chen, L. Buffer Compliance Control of Space Robots Capturing a Non-Cooperative Spacecraft Based on Reinforcement Learning. *Appl. Sci.* **2021**, *11*, 5783. [CrossRef]
9. Chalon, M.; Wedler, A.; Baumann, A.; Bertleff, W.; Beyer, A.; Butterfaß, J.; Grebenstein, M.; Gruber, R.; Hacker, F.; Kraemer, E.; et al. Dexhand: A Space Qualified Multi-Fingered Robotic Hand. In Proceedings of the 2011 IEEE International Conference on Robotics and Automation (ICRA), Shanghai, China, 9–13 May 2011; pp. 2204–2210. [CrossRef]
10. Chalon, M.; Maier, M.; Bertleff, W.; Beyer, A.; Bayer, R.; Friedl, W.; Neugebauer, P.; Obermeier, T.; Sedlmayr, H.J.; Seitz, N.; et al. Spacehand: A Multi-Fingered Robotic Hand for Space. In Proceedings of the 13th Symposium on Advanced Space Technologies in Robotics and Automation (ASTRA), Noordwijk, The Netherlands, 11–13 May 2015; pp. 1–8.
11. Nam, U.W.; Park, W.K.; Youn, S.; Kwak, J.; Sohn, J.; Moon, B.; Lee, J.; Choi, Y.J.; Kim, J.; Kim, S.; et al. Initial Results of Low Earth Orbit Space Radiation Dosimeter on Board the Next Generation Small Satellite-2. *J. Astron. Space Sci.* **2024**, *41*, 195–208. [CrossRef]
12. Choi, T.; Choi, S.; Jun, B.; Park, J.-H.; Won, D.; Lee, D.-H. Cosmic Gripper-1: 3-Finger Gripper for Space Tasks. In Proceedings of the 2025 International Conference on Space Robotics (iSpaRo), Sendai, Japan, 1–4 December 2025. [CrossRef]
13. Bicchi, A. Hands for Dexterous Manipulation and Robust Grasping: A Difficult Road toward Simplicity. *IEEE Trans. Robot. Autom.* **2000**, *16*, 652–662. [CrossRef]
14. Ciocarlie, M.; Allen, P. Hand Posture Subspaces for Dexterous Robotic Grasping. *Int. J. Robot. Res.* **2009**, *28*, 851–867. [CrossRef]
15. Dollar, A.M.; Howe, R.D. The Highly Adaptive SDM Hand: Design and Performance Evaluation. *Int. J. Robot. Res.* **2010**, *29*, 585–597. [CrossRef]
16. Calli, B.; Singh, A.; Walsman, A.; Srinivasa, S.; Abbeel, P.; Dollar, A.M. Benchmarking in Manipulation Research: Using the Yale-CMU-Berkeley Object and Model Set. *IEEE Robot. Autom. Mag.* **2015**, *22*, 36–52. [CrossRef]
17. Backus, S.B.; Dollar, A.M. An Adaptive Three-Fingered Prismatic Gripper with Passive Rotational Joints. *IEEE Robot. Autom. Lett.* **2016**, *1*, 668–675. [CrossRef]
18. German Aerospace Center (DLR). DEXHAND. Available online: https://www.dlr.de/en/rm/research/robotic-systems/hands/dexhand-2012-2015 (accessed on 13 May 2026).
19. German Aerospace Center (DLR). SpaceHand. Available online: https://www.dlr.de/en/rm/research/robotic-systems/hands/spacehand-2015-2018 (accessed on 13 May 2026).
20. Jacobsen, S.C.; Wood, J.E.; Knutti, D.F.; Biggers, K.B. The UTAH/MIT Dextrous Hand: Work in Progress. *Int. J. Robot. Res.* **1984**, *5*, 21–50. [CrossRef]
21. Salisbury, J.K.; Craig, J.J. Articulated Hands: Force Control and Kinematic Issues. *Int. J. Robot. Res.* **1982**, *1*, 4–17. [CrossRef]
22. Palli, G.; Borghesan, G.; Melchiorri, C. Modeling, Identification, and Control of Tendon-Based Actuation Systems. *IEEE Trans. Robot.* **2012**, *28*, 277–290. [CrossRef]
23. Jang, T.S.; Rhee, J. Domestic Study Trend of Radiation Shielding Structure for Space. *Aerosp. Ind. Technol. Trends* **2017**, *15*, 109–117. (In Korean)
24. Wilson, J.W.; Miller, J.; Konradi, A.; Cucinotta, F.A. (Eds.) *Shielding Strategies for Human Space Exploration*; NASA Conference Publication 3360; NASA: Washington, DC, USA, 1997.
25. Wang, M.; Wang, Q.; Xiao, Y.; Wang, M.; Wang, J.; Wang, H.; Chen, Z. Review of Passive Shielding Materials for High-Energy Charged Particles in Earth's Orbit. *Materials* **2025**, *18*, 2558. [CrossRef] [PubMed]
26. Daneshvar, H.; Ghordoei Milan, K.; Sadr, A.; Sedighy, S.H.; Malekie, S.; Mosayebi, A. Multilayer Radiation Shield for Satellite Electronic Components Protection. *Sci. Rep.* **2021**, *11*, 20657. [CrossRef] [PubMed]
27. Thomsen, D.L.; Jordan, T.M.; Milic, L.; Girard, W. Shielding Considerations for CubeSat Structures During Solar Maximum. In Proceedings of the 37th Annual Small Satellite Conference, Logan, UT, USA, 5–10 August 2023; SSC23-X-01. Available online: https://digitalcommons.usu.edu/cgi/viewcontent.cgi?article=5639&context=smallsat (accessed on 13 May 2026).
28. Lee, D.-H.; Park, J.-H.; Park, S.-W.; Baeg, M.-H.; Bae, J.-H. KITECH-Hand: A Highly Dexterous and Modularized Robotic Hand. *IEEE/ASME Trans. Mechatron.* **2017**, *22*, 876–887. [CrossRef]
29. Lee, Y.; Lee, J.; Jung, D.; Park, D.I.; Kim, U. INDEX Gripper: Industrial Dexterous Robotic Gripper Capable of All-Orientational Object Manipulation. *IEEE/ASME Trans. Mechatron.* **2025**, *30*, 123–134. [CrossRef]
30. Nagase, J.-Y.; Saga, N.; Satoh, T.; Suzumori, K. Development and Control of a Multifingered Robotic Hand Using a Pneumatic Tendon-Driven Actuator. *J. Intell. Mater. Syst. Struct.* **2012**, *23*, 345–352. [CrossRef]
31. Bae, J.-H.; Park, S.-W.; Kim, D.; Baeg, M.-H.; Oh, S.-R. A Grasp Strategy with the Geometric Centroid of a Groped Object Shape Derived from Contact Spots. In Proceedings of the 2012 IEEE International Conference on Robotics and Automation (ICRA), Saint Paul, MN, USA, 14–18 May 2012; pp. 2133–2138.
32. European Cooperation for Space Standardization (ECSS). *Space Engineering—Verification*; ECSS-E-ST-10-02C Rev.1; European Cooperation for Space Standardization (ECSS): Noordwijk, The Netherlands, 2018.

33. National Aeronautics and Space Administration (NASA). *NASA Systems Engineering Handbook*, Rev. 2; NASA/SP-2016-6105; National Aeronautics and Space Administration (NASA): Washington, DC, USA, 2016. Available online: https://ntrs.nasa.gov/citations/20230011128 (accessed on 13 May 2026).
34. Alciatore, D.; Ng, C. Determining Manipulator Workspace Boundaries Using the Monte Carlo Method and Least Squares Segmentation. In Proceedings of the ASME Design Engineering Technical Conferences (DETC), Minneapolis, MN, USA, 11–14 September 1994; Paper No. DETC1994-0316; pp. 141–146. Available online: https://www.engr.colostate.edu/~dga/documents/papers/workspace.pdf (accessed on 19 May 2026).
35. Yoshikawa, T. Manipulability of Robotic Mechanisms. *Int. J. Robot. Res.* **1985**, *4*, 3–9. [CrossRef]
36. Agostinelli, S.; Allison, J.; Amako, K.A.; Apostolakis, J.; Araujo, H.; Arce, P.; Asai, M.; Axen, D.; Banerjee, S.; Barr, G.J.; et al. Geant4—A Simulation Toolkit. *Nucl. Instrum. Methods Phys. Res. Sect. A* **2003**, *506*, 250–303. [CrossRef]
37. Vette, J.I. The AE-8 Trapped Electron Model Environment. In *NSSDC/WDC-A-R&S*; 91-24; NASA Goddard Space Flight Center: Greenbelt, MD, USA, 1991.
38. Heynderickx, D.; Quaghebeur, B.; Wera, J.; Daly, E.J.; Evans, H.D.R. New Radiation Environment and Effects Models in the European Space Agency's Space Environment Information System (SPENVIS). *Space Weather* **2004**, *2*, S10S03. [CrossRef]
39. ESA/BIRA-IASB. Space Environment Information System (SPENVIS). Available online: https://www.spenvis.oma.be/ (accessed on 19 May 2026).
40. Seltzer, S.M. Updated Calculations for Routine Space-Shielding Radiation Dose Estimates: SHIELDOSE-2. In *NIST Publication NISTIR 5477*; National Institute of Standards and Technology: Gaithersburg, MD, USA, 1994.
41. *ISO 9283:1998*; Manipulating Industrial Robots—Performance Criteria and Related Test Methods. International Organization for Standardization: Geneva, Switzerland, 1998.
42. Kruskal, W.H.; Wallis, W.A. Use of Ranks in One-Criterion Variance Analysis. *J. Am. Stat. Assoc.* **1952**, *47*, 583–621. [CrossRef]
43. Dunn, O.J. Multiple Comparisons Using Rank Sums. *Technometrics* **1964**, *6*, 241–252. [CrossRef]
44. DSM Dyneema. *Comprehensive Factsheet: Ultra High Molecular Weight Polyethylene Fiber from DSM Dyneema*; Ref. CIS YA100; DSM Dyneema B.V.: Heerlen, The Netherlands, 2008.
45. Guzik, A.T.; Benafan, O. *Design and Development of CubeSat Solar Array Deployment Mechanisms Using Shape Memory Alloys*; NASA/TM-2018-219914; NASA Glenn Research Center: Cleveland, OH, USA, 2018.
46. Wu, H.; Yin, M.; Xu, Z.; Zhao, Z.; Han, W. Transmission Characteristics Analysis and Compensation Control of Double Tendon-Sheath Driven Manipulator. *Sensors* **2020**, *20*, 1301. [CrossRef] [PubMed]
47. Gao, Q.; Li, J. A Feedforward Tendon-Elongation Compensator for Tendon-Sheath Mechanisms with Arbitrary and Time-Varying Transmission Routes in Three-Dimensional Space. *Biomim. Intell. Robot.* **2026**, *6*, 100278. [CrossRef]
48. Shapiro, W.; Murray, F.; Howarth, R.; Fusaro, R. *Space Mechanisms Lessons Learned Study, Volume I: Summary*; NASA Technical Memorandum 107046; NASA Lewis Research Center: Cleveland, OH, USA, 1995.
49. Rivera, A.; Stewart, A. Study of Spacecraft Deployables Failures. In Proceedings of the 19th European Space Mechanisms and Tribology Symposium (ESMATS), Online, 20–24 September 2021.
50. Kim, D.Y.; Choi, H.S.; Lim, J.H.; Kim, K.W.; Jeong, J.W. Experimental and Numerical Investigation of Solar Panels Deployment with Tape Spring Hinges Having Nonlinear Hysteresis with Friction Compensation. *Appl. Sci.* **2020**, *10*, 7902. [CrossRef]
51. Kalaycioglu, S.; Zheng, W.; Giray, M. Robotics Evaluation and Characterization (REACH) of the SSRMS. In Proceedings of the International Advanced Robotics Programme (IARP), Montreal, QC, Canada, 6–8 July 1994.

Disclaimer/Publisher's Note: The statements, opinions and data contained in all publications are solely those of the individual author(s) and contributor(s) and not of MDPI and/or the editor(s). MDPI and/or the editor(s) disclaim responsibility for any injury to people or property resulting from any ideas, methods, instructions or products referred to in the content.